Author Manuscript

Statistical Characterization of GITM Thermospheric Horizontal Winds in Comparison to GOCE Estimations

Daniel A. Brandt[1], **Aaron J. Ridley**[2]

[1]Michigan Tech Research Institute, Michigan Technological University
[2]Department of Climate and Space Science and Engineering, University of Michigan - Ann Arbor

Key Points:

- Cross-track horizontal winds from GOCE are compared to GITM for Jan-Oct 2013.
- GITM captured the overall distribution of horizontal winds, but with lower means than GOCE.
- GITM overpredicts horizontal wind just outside the equatorial ionization anomaly regions.

Corresponding author: Daniel A. Brandt, branddan@umich.edu

This is the author manuscript accepted for publication and has undergone full peer review but has not been through the copyediting, typesetting, pagination and proofreading process, which may lead to differences between this version and the Version of Record. Please cite this article as doi: 10.1029/2021SW002922.

This article is protected by copyright. All rights reserved.

Author Manuscript

Abstract

Characterization of the thermospheric horizontal wind is an important challenge in atmospheric modeling due to its vital role in the transport of densities and energy, associations with the diurnal tide, and interplay with vertical winds that drive changes in the thermosphere neutral composition. The mechanisms and drivers that underlie the physics of thermospheric horizontal winds remain under investigation and, to date, no comprehensive statistical study between thermospheric winds generated by a physics-based atmospheric model and those retrieved from satellite measurements has been performed. Comparisons between cross-track horizontal winds from a 10-month run of GITM and those derived from the Gravity field and steady-state Ocean Circulation Explorer (GOCE) satellite show that GITM did best modeling horizontal winds in the polar zone but overestimated horizontal wind speeds at midlatitudes just outside of the equatorial ionization anomaly region. GITM's wind response to AE was best at polar noon and worst in the midnight auroral zone, its ability to capture seasonality was best in the northern high latitudes and worst in the southern high latitudes, and GITM displayed less wind variability as a function of F10.7 than GOCE, matching it best for F10.7$>\sim 150$. Discrepancies in GITM's performance may be explained by inaccurate modeling of ion drift, ion drag, and electron densities.

Plain Language Summary

Modeling the behavior of the horizontal wind in the thermosphere is an important challenge, since the horizontal wind plays a major role in the dynamics of the thermosphere. Horizontal winds are important because they change the neutral composition of the atmosphere and redistribute energy from the high latitudes towards the equator. While there exist several physics-based models of the atmosphere capable of modeling horizontal winds, there has not yet been a detailed statistical study comparing model results to horizontal wind data from satellites. Data collected by the Gravity field and steady-state Ocean Circulation Explorer (GOCE) satellite show that behavior of the horizontal wind is related to geomagnetic activity, magnetic latitude, and magnetic local time. We evaluated the capability of the Global Ionosphere-Thermosphere Model (GITM) to capture that behavior through a statistical analysis of the horizontal wind. We show that GITM performs best at higher levels of activity in the auroral region and worst just outside the equatorial anomaly region.

1 Introduction

Changes in atmospheric density and composition can drive horizontal winds in the thermosphere. These winds redistribute energy in response to temperature changes, and play an important role in the global thermospheric circulation. The importance of horizontal winds can be seen in that their divergence and convergence can drive vertical flows, density and composition changes, and changes in temperature (Prlss (1980), (Smith, 1998), and Burns et al. (1991)). Their interactions with ions like O_2^+, NO^+ and O^+ can drive frictional temperature changes as well as field-aligned flows (Guo et al., 2018), and they can push ions across field lines, driving electrodynamical changes in the F-region ionosphere (Billett et al., 2020). While it is clear that winds are critical in describing the thermosphere and ionosphere, there are not many measurements of them, and model validation studies of the winds are few and far between. Since the neutral wind is an important means by which the atmosphere reacts to momentum and heat transfer (Johnson et al., 1995), it plays a vital role in the composition of the thermosphere, especially at the low and middle latitudes (Burns et al., 1989). Convergence and divergence of horizontal winds is also an important mechanism that can produce vertical winds (Rishbeth & Müller-Wodarg, 1999). Therefore, improving understanding of the horizontal winds

This article is protected by copyright. All rights reserved.

Author Manuscript

will lead to an improved understanding of how winds behave in the thermosphere and how thermospheric circulation is impacted by various environmental conditions.

1.1 Horizontal Wind Observation Methods

There are a variety of methods for measuring horizontal winds in the thermosphere. Many, such as specular meteor radars and Doppler lidars, are exclusively used on the ground, while others, such as Fabry-Perot interferometers (FPIs), have been used on both the ground and onboard satellites. While each of these methods have their own particular benefits, wind measurements derived from highly-accurate accelerometer measurements onboard low Earth orbit (LEO) satellites present a unique opportunity to study thermospheric winds in depth by virtue of being within the medium of interest itself.

Specular meteor radars detect plasma trails from incoming meteors when their paths lie perpendicular to the radar beam (Ceplecha et al., 1998). Measuring the average Doppler shift allows an observer to infer neutral wind speeds along the radar's line of sight, providing an inexpensive means of generating a dataset of horizontal winds for model development. Recent developments in meteor radar techniques have allowed large radars to be used by following reflections from plasma irregularities that develop from many meteor trails instead of following a single trail with a small radar, and have yielded observations showing wind speeds over 100 m/s between 93 and 110 km using a large VHF radar (Oppenheim et al. (2000) and Oppenheim et al. (2009)). Improvements in calibration and detection techniques have also granted the capability of deriving useful information from nonspecular meteor trails ((Zhao et al., 2011)) and observations from multilink configurations where the radar receivers are not located at the same location as the transmitters ((Chau & Clahsen, 2019)). While this technique can produce high-resolution observations of horizontal winds, it is limited to the upper mesosphere and lower thermosphere and requires as a large VHF radar with interferometric capability.

Horizontal wind measurements are also frequently obtained from Fabry-Perot Interferometer (FPI) observations (Martinis et al. (2001), Oyama et al. (2010), Conde and Smith (1998), and Meriwether et al. (2011)). The speed and direction of the horizontal winds can be obtained by observing the same thermospheric volume at orthogonal look directions from two sites. It is customary to assume a vertical zero-wind reference measurement (J. J. Makela et al. (2013), and Biondi (1984)), or use a stable calibration source, such as a frequency-stabilized HeNe laser (J. Makela et al., 2012). FPIs have been used to show the relationship between horizontal convergence/divergence and changes in the vertical flow (Biondi & Sipler, 1985). Under geomagnetically quiet conditions in the midlatitudes, FPI measurements routinely show wind speeds up to 50 m s^{-1} in the zonal direction and up to 100 m s^{-1} in the meridional direction (Jiang et al., 2018). FPI measurements have additionally shown increased zonal flow and stronger southward meridional flow as a function of increasing altitude, as well as greater absolute wind speeds during the winter (Yuan et al., 2013). They have also been used to study the impact of gravity waves and atmospheric airglow on wind velocity observations in comparison to those obtained with radar techniques (Fujii et al., 2004).

Doppler lidars have been used to study wind and temperature in the mesopause region by detecting the Doppler shift of atomic spectral lines of mesospheric metals such as Na (Bowman et al. (1969), fang Du et al. (2017) and Philbrick et al. (2021)). This technique has seen most applicability using broadband lidars to observe the mesopause region and below, but notable observations of the existence of detectable metals within the lower thermosphere (Gardner et al. (1999), Chu et al. (2011), and Gao et al. (2015)) and the usage of a narrow-band Lidar has enabled observation of winds up to 140 km using this method. Doppler lidar measurements have been shown to be consistent with past rocket measurements (A. Z. Liu et al., 2016).

This article is protected by copyright. All rights reserved.

Author Manuscript

Satellites in low Earth orbit (LEO) present another source for thermospheric horizontal wind measurements. FPIs have been used aboard satellites such as Dynamics Explorer 2 (DE-2), where they were primarily used to measure the meridional component of the upper thermospheric neutral wind (Killeen et al., 1992). A FPI was also flown aboard the Upper Atmosphere Research Satellite (UARS), where it observed an amplitude of the diurnal tide in the meridional wind larger than that observed by ground-based meteor radars by more than a factor of 2 (Khattatov et al., 1997). The Thermosphere-Ionosphere-Mesosphere Energetics and Dynamics (TIMED) satellite also carries onboard a limb-scanning FPI known as the TIMED Doppler Interferometer (TIDI), which has been used to study migrating diurnal and semidiurnal tides and consistently reproduces ground-based radar observations of the wind (Killeen et al., 2006). The Gravity field and steady-state Ocean Circulation Explorer (GOCE) is another source of horizontal wind data (Floberghagen et al., 2011). The satellite was launched on 17 March 2009, used an ion thruster to sustain its orbit at $\sim$250 km at 96.7° inclination, and reentered the Earth's atmosphere on 11 November 2013 (Strugarek et al., 2019). GOCE's orbit was near sun-synchronous and had a dusk ascending node, and a dawn descending node. GOCE's main payload was the Electrostatic Gravity Gradiometer (EGG), a set of six 3-axis accelerometers mounted in a diamond configuration. The accelerometers of the EGG were 100 times more sensitive than any others previously flown, such as the SuperSTAR accelerometer onboard the GRACE spacecraft (Touboul, 2003). GOCE accelerometer data have been used to investigate the wave coupling between the lower and middle thermosphere (Gasperini et al., 2015), probe the mechanisms driving an eastward wind jet in the evening sector and westward wind jet in the morning sector as well characterizing seasonal variation of the wind (H. Liu et al., 2016), and improve handling of the energy accommodation coefficient to reduce discrepancies when compared to ground-based measurements (Visser et al., 2019a).

1.2 Atmospheric Models

Several atmospheric models have been developed and used to simulate the horizontal wind in the thermosphere. The most prominent of these is the Horizontal Wind Model (HWM), which is currently the most comprehensive empirical model and describes the atmosphere's vector wind fields from the surface to the exobase as a function of latitude, longitude, altitude, day of year, and time of day. It additionally provides a time-dependent, observationally based, global empirical specification of the upper atmospheric tides and general circulation patterns (Drob et al., 2015). The first version of HWM (HWM87) was generated from thermospheric wind data obtained from the Atmosphere Explorer E and DE-2 satellites, and was limited to above 220 km (Hedin et al., 1988). A subsequent version (HWM90) saw the incorporation of ground-based incoherent scatter radar and FPI data and extension down to 100 km (Hedin et al., 1991), and was succeeded by HWM07, which covers altitudes from the surface to the exosphere and includes representations of zonal means circulation, stationary waves and migrating tides (Drob et al., 2008). The most recent version is HWM14, which incorporates 630 nm FPI data and GOCE cross-track winds (Drob et al., 2015). Due to the limitations of HWM in modeling storm-time wind activity, a global empirical disturbance wind model (DWM07) was developed that represents averaged geospace-storm-induced perturbations of the upper thermospheric neutral winds, based on data from the Upper Atmospheric Research Satellite, the Dynamics Explorer 2 satellite, and seven ground-based FPIs. A more recent model is the Magnetic mEridional NeuTrAl Thermospheric (MENTAT) model, which was developed from a global database of ionosonde h_mF_2 observations spanning the years 1961 to 1990, that captures solar cycle wind variation other empirical models fail to reproduce (Dandenault, 2018). The High-latitude Thermospheric Wind Model (HL-TWiM) is another recently-developed empirical model that specifies horizontal neutral winds in the F region at high-latitudes as a function of day of year, latitude, longitude, local time, and geomagnetic activity. It was developed from a several decades of F region FPI measurements and is

This article is protected by copyright. All rights reserved.

Author Manuscript

able to capture the semiannual oscillation-like behavior of winds measured by GOCE (Dhadly et al., 2019).

Physics-based models of the upper atmosphere also specify the horizontal neutral winds across the globe. The Coupled-Magnetosphere-Ionosphere-Thermosphere (CMIT) Model is a physics-based model that consists of three codes: (1) the Lyon-Fedder (LFM) global magnetospheric MHD code, (2) the Rice Convection Model, and (3) the Thermosphere Ionosphere Electrodynamic General Circulation Model (TIEGCM). A detailed description of the model and the coupling procedure can be found in Wiltberger et al. (2004) and Wang et al. (1999). CMIT was used to study altitude variations of the horizontal wind during geomagnetic storms, validated the assumption of a shearless vertical profile of the horizontal winds in low and middle latitudes during quiet times, and showed during storm time that enhancement of momentum advection and pressure gradient forces can create large vertical shears in the horizontal winds (Wang et al., 2008). The Global-Ionosphere Model (GITM) (Ridley et al., 2006) is another physics-based model, and has been used to investigate the effects of electric potential and auroral precipitation on thermospheric wind patterns by conducting multiple simulations of a substorm event on 24 November 2012 using various combinations, revealing that GITM overestimated the magnitude of the neutral winds at GOCE altitudes (Liuzzo et al., 2015). A year-long run of GITM evaluated against nighttime neutral wind data from FPIs also indicated that GITM performs poorly at capturing spatial structure and day-to-day variability of the horizontal winds (Harding et al., 2019). While each of these models has been used to study different aspects of thermospheric horizontal winds, there is yet to be a study involving use of these models to statistically characterize thermospheric horizontal wind behavior over an extended period.

1.3 Motivation

Horizontal winds have been studied to understand thermospheric climatology represented by annual/diurnal variation and semidiurnal tidal variations (Yao et al., 2015), derived from observations of neutral and electron densities from satellite data to estimate wind behavior at low latitudes (Gasperini et al., 2016), and observed with a meteor radar to investigate the efficacy of that detection method, study wind seasonality, and the reveal importance of stationary planetary waves (Korotyshkin et al., 2019). However, studies involving modeling of the horizontal winds have primarily involved validation of HWM, which recently was used to investigate the tracking of sporadic E field-aligned irregularities as a probe of thermospheric winds (Helmboldt & Taylor, 2020), and GITM being used to investigate how the magnitude and temporal variations of ion drifts affect Joule heating in relation to the vertical wind structure (Yiit & Ridley, 2011). However, to date, the horizontal winds in GITM have not been validated extensively in any way. In order to elucidate the role horizontal winds play in thermosphere dynamics it is useful to investigate their behavior over several parameters, including magnetic local time, magnetic latitude, season, and magnetic activity, which can be represented adequately well by the auroral electrojet index (AE) (Davis and Sugiura (1966) and Weygand et al. (2014)). This approach has been done with the standard deviation of the vertical wind $\sigma(V_z)$ in Visser et al. (2019b), but has heretofore not been applied to any studies of the horizontal wind.

The purpose of this paper is to characterize the capability of GITM to model thermospheric horizontal wind behavior as a function of magnetic latitude and geomagnetic activity that has been observed in data derived from linear accelerometers. This was done by comparing GITM's outputs along the orbit track of the GOCE satellite and performing statistical analysis between the datasets after separating them into categories based on magnetic latitude, magnetic local time, and auroral electrojet index. This statistical analysis aims to reveal areas for improvement of GITM for the purposes of its continued development.

This article is protected by copyright. All rights reserved.

Author Manuscript

2 Methodology

Statistical analysis involved comparisons between GOCE cross-track (horizontal) winds and GITM winds along the GOCE orbit. GOCE winds derived from accelerometer data were obtained from TU Delft. Doornbos et al. (2010) describes the process of how wind data was obtained, in which measured accelerations were used to determine a net force and torque acting on the satellite. Models described in Doornbos (2011) and Visser et al. (2018) were combined with measurements and housekeeping data to estimate the forces and torques on the spacecraft caused by the gravity gradient, magnetic attitude control, and other equipment. The residual force and torque were found by subtracting the model output from the measurement. This residual force and torque were assumed to be entirely aerodynamic, and an aerodynamic model was constructed to match it by changing the direction of the incoming flow. The wind vector was thus defined as the difference between the flow and the orbital plus co-rotation velocities. The acceleration due to drag on the spacecraft can then be written in the following form:

$$\vec{a} = -\frac{1}{2}\rho\frac{A}{m}C_D\left(\vec{v_o} - \vec{v_w}\right)^2\left(\widehat{v - v_w}\right) \tag{1}$$

where the ρ is the local thermospheric density, A is the spacecraft cross-sectional area, m is the spacecraft mass, C_D is the drag coefficient, $\vec{v_o}$ is the orbital velocity of the spacecraft, and $\vec{v_w}$ is the velocity of the thermospheric wind, which includes velocities in the along-track, cross-track, and cross-vertical directions, as well as contributions from co-rotation. It is extraordinarily difficult to separate change in ρ versus change in $v_o - v_{\text{along}}$, so it is customary to assume that v_{along} is negligible given that $v_o >> v_{\text{along}}$. For more information, this algorithm is described in detail in Visser et al. (2019a).

Table 1. GITM Parameters for the Horizontal Wind Validation Study

Parameter	**Value**
Eddy Diffusion Coefficient	100
Eddy Pressure Lower	0.0050
Eddy Pressure Upper	0.0005
Photoelectron Heating Efficiency	0.02
Neutral Heating Efficiency	0.05
Thermal Conduction (Molecular)	3.6×10^{-4}
Thermal Conduction (Atomic)	5.6×10^{-4}
Thermal Conduction Power	0.69
AUSMSolver	True
CFL	0.80
Limiter	MC, 2.0
Dynamo High Lat. Boundary	45.0
Improved Ion Advection	True
Nighttime Ion B.C.s	True
Minimum TEC for Ion B.C.s	2.0

This article is protected by copyright. All rights reserved.

Author Manuscript

GITM was used to model horizontal winds, and was run from January to November 2013 with the conditions in Table 1. GITM (Ridley et al., 2006) is a three-dimensional, spherical, parallel code that models the thermosphere-ionosphere system using a stretched altitude grid. Its lower boundary is 100 km and it includes diurnal, semi-diurnal, and ter-diurnal tides specified by the NRLMSISE-00 atmospheric density model (Picone et al., 2002) and the Horizontal Wind Model (Drob et al., 2008). It allows for non-hydrostatic solutions and solves for the neutral, ion, and electron temperatures, the bulk horizontal neutral winds, the vertical velocity of the individual species, and ion and electron velocities. The code can use a dipole magnetic field, a tilted dipole, or the IGRF magnetic field with the APEX coordinate system (Richmond, 1995). The primary drivers of the thermosphere and ionosphere in GITM are solar EUV modeled by the Flare Irradiance Spectral Model (FISM) (Chamberlin et al. (2007) and Chamberlin et al. (2008)) and high-latitude electrodynamics, which are specified by the Weimer (2005) electrodynamic potential patterns. The potential patterns are driven by time-delayed IMF and solar wind measurements from the Advanced Composition Explorer (ACE) satellite and the Fuller-Rowell and Evans (1987) particle precipitation patterns driven by hemispheric power estimated by the LEO satellites operated by the National Oceanographic and Atmospheric Administration (NOAA). GITM is also equipped with a potential dynamo solver (Vichare et al., 2012).

GITM computes both the meridional (north) and zonal (east) components of the horizontal wind, while GOCE measured the winds perpendicular to its orbit in the horizontal and vertical directions. In order to compare GITM to GOCE, only the GITM wind components perpendicular to the GOCE orbit were considered (i.e., each of the north and east component of the modeled wind was dotted with the horizontal vector indicating the local orthogonal direction of GOCE's orbit.) This means that near the equator, there is almost no north component of the winds measured by GOCE, due to it moving almost completely in the north/south direction. At high latitudes, the east component is reduced significantly, since GOCE is orbiting in an almost east/west direction. By taking this into account with the GITM results, the winds can more-accurately be compared. As the horizontal wind in GITM was extracted along the GOCE orbit, both the GITM results and the GOCE measurements have the same 10-second temporal resolution. As the GOCE cross-track wind measurements have associated errors, some measurements may constitute outliers in the data and be too uncertain. Therefore, for wind measurements in excess of 25 m/s, if the associated error was greater than 25 m/s and the absolute value of the GOCE cross-track wind measurement was less than the associated error, the wind data were discarded.

Figure 1 shows a comparison between cross-track winds in geographic coordinates estimated by GOCE and those simulated by GITM. Because of the complexity of the measurements, the cross-track winds are broken into east (zonal) and north (meridional) components for the ascending (near dusk) and descending (near dawn) phases. The magnitude of the cross-track wind is also shown, in order to provide a context for the rest of the study. Data from March 10-19, 2013 are shown. During most of the time, the geophysical conditions are relatively low, except for March 17, in which there is a geomagnetic storm, and all components of the winds are seen to be perturbed.

Qualitatively, there are several regions of general agreement and disagreement between the GITM results and GOCE measurements:

- In both the east and north winds in ascending and descending phases, the direction of the GITM winds matched the direction of the GOCE winds, except in very specific locations (such as in the high-latitudes, where there was a shift between the east/west shear) or when the winds were very weak, such as in the north wind at mid- and low-latitudes.

This article is protected by copyright. All rights reserved.

Author Manuscript

- In the east ascending winds (a), GITM captured the overall east wind at low- and mid-latitudes, but not the actual structure, and it overestimated the magnitude in most locations. The zonal winds at low latitudes near dusk are primarily driven by day-to-night pressure gradients and are modulated by viscosity and ion drag. At higher latitudes (both north and south), GITM underestimated the east wind, but captured regions of strong west wind, most likely driven by high-latitude ion drag.
- In the east descending winds (b), GITM significantly overestimated the west winds at mid- and low-latitudes, possibly due to too weak of viscosity or ion drag. The higher-latitude winds in GITM showed winds closer to zero more often than GOCE.
- In the wind magnitude (e, f), GITM had larger wind speeds at mid- and low-latitudes and smaller wind speeds at higher latitudes. This was especially true in the transition zone between the high-latitude and mid-latitude flows, in which GITM showed a region of very low flows, while GOCE had a narrower-to-nonexistent region of low flows.

In order to conduct a more quantitative analysis, we closely followed the statistical analysis of Visser et al. (2019b) and applied it to the cross-track horizontal wind magnitude (termed V_x) only, instead of attempting to compare it to both the east and north wind. As shown in Figure 1, the directionality of the winds produced by GITM was very good, so only the magnitude of the cross-track winds was compared in subsequent analysis. GITM V_x results were compared to GOCE V_x data in terms of their probability distributions calculated over bins with a width of 1 m/s, in order to identify GITM's biases as a function of AE and MLAT. The 25th, 50th, and 75th percentiles were calculated for each distribution in order to inspect GITM's overall performance in comparison to GOCE at low, median, and high wind speeds over various wind drivers. We considered the effects of several controlling parameters on the comparison: magnetic latitude (MLAT), magnetic local time (MLT), day-of-the-year (DOY), and geomagnetic activity. We used the minute-by-minute Auroral Electroject (AE) Index to quantify geomagnetic activity. This geomagnetic index is particularly relevant given that acceleration of the neutral wind has been observed in response to electrojet intensification (Cai et al., 2019). We calculated probability densities in three magnetic latitude ranges: mid-latitudes (30$\leq$60°), auroral latitudes (60$\leq$80°) and polar cap latitudes (80$\leq$90°). As in Visser et al. (2019b) and Innis and Conde (2002), we further restricted each MLAT range according to the following AE bounds: AE$\leq$250 (low activity), 250<AE$\leq$500 (moderate activity), and AE>500 (high activity).

In order to compare and contrast how GITM's V_x responded to different parameters and compare that responsiveness to that of the GOCE data, we again mirrored the method of Visser et al. (2019b) and distributed the data over bins of AE, MLAT, MLT, DOY, and F10.7, and plotted the 25th, 50th, and 75th percentiles of V_x. We completed our analysis with a series of implications and future steps.

3 Results

The neutral winds are controlled by forces that are ordered in both geographic coordinates (e.g., gradient in the day-to-night pressure, viscosity, and Coriolis forces) and magnetic coordinates (e.g., ion drag). Therefore, no matter which coordinate system is chosen to plot the data, there is a diurnal variation that is caused by the Earths magnetic field rotating through the day (as shown in Figure 1). This variation is mostly driven by the ions being tied to the magnetic field structure and dragging the neutrals faster (at high-latitudes due to magnetospheric forcing) or slower (at low-latitude, due to the magnetic fields not moving). We have chosen to quantitatively compare the results in modified Apex coordinates to minimize the effect, but it leads to other effects, such as a lack of results in the region around the dipole magnetic equator. This is a projection

This article is protected by copyright. All rights reserved.

Author Manuscript

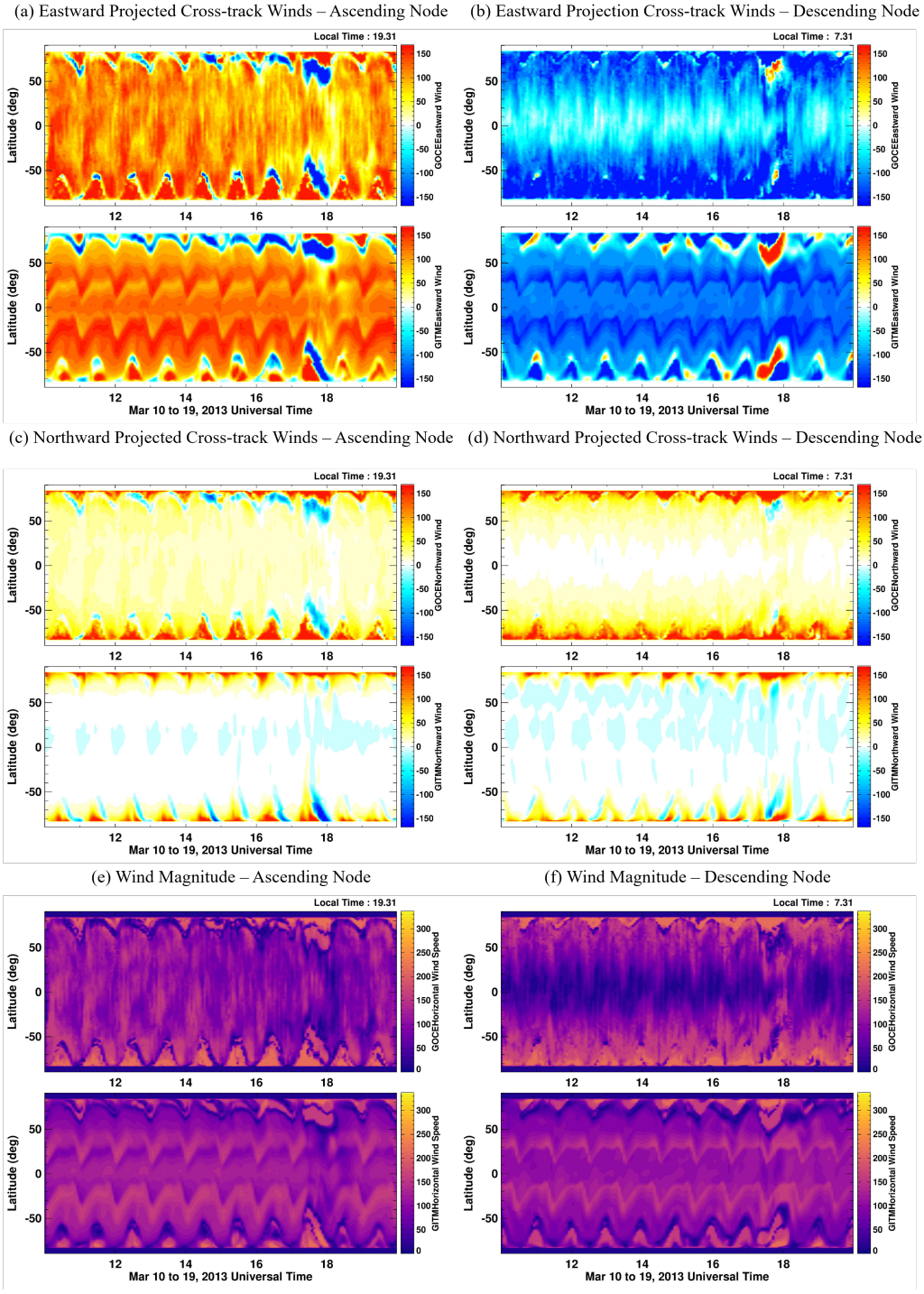


Figure 1. Comparisons between GOCE (top plots) and GITM (bottom plots) cross-track winds in geographic coordinates. The east-component (a, b), north-component (c, d), and magnitude (e, f) are shown for the ascending (a, c, e) and descending (b, d, f) nodes.

effect due to the choice of using a reference altitude of 100 km for calculating the Apex latitude. Field-lines are traced from the chosen position, in this case GOCE's altitude of ∼250 km, out to the apex of the field-line, and then back to the reference altitude,

This article is protected by copyright. All rights reserved.

Author Manuscript

providing the dipole latitude of that point (Richmond, 1995). Therefore, field-lines that pass through ∼250 km do not sample 0° Apex magnetic latitude.

Figures 2 and 3 show the horizontal cross-track wind speed from GITM and GOCE. During the entire time period considered, both GITM and GOCE horizontal winds showed greater speeds in the high-latitude region and lesser speeds in the mid-latitudes, in both hemispheres for both the ascending and descending nodes.

By inspection, GITM demonstrated difficulty in capturing finer latitudinal structures in the horizontal wind speed, and placed a morphological feature at $\pm 20° - 30°$, just outside of the Equatorial Ionization Region (EIA), which typically features as a band of higher ion and electron densities in the vicinity of $\pm 15°$ (Hsu et al., 2014). GITM also struggled with capturing some of the seasonal variation in the horizontal wind speeds shown in the GOCE data. This is most evident in the mid-latitudes for the descending node (Figure 3, near dawn): The GOCE data showed that higher wind speeds begin to extend from the auroral to the equatorial region throughout the summer in the Northern Hemisphere, which GITM failed to capture, as it underestimated the winds during those times in that region. Conversely, for the ascending node (Figure 2, near dusk), during that same time period, GITM *overestimated* the horizontal winds in the same latitude region. For both the ascending and descending node throughout the entire year, GITM generally overestimated the horizontal wind speeds in the low- and mid-latitudes in both hemispheres.

One explanation for this overestimation could be that GITM's electron density may have been too weak during this time period. Figure 4 shows the vertical total electron content measured by the world-wide distribution of Global Navigation Satellite Services (GNSS) receivers and modeled by GITM. This comparison shows that GITM's electron density was most likely too low across the globe, and especially low on the dayside. The measurements showed strong electron density peaks extending to approximately $\pm 30°$ latitude, while GITM's anomaly peaks were much closer to the equator. Further, the density at mid-latitude in GITM was also a bit lower than the measurements. This would have driven a consistently lower ion drag across the dayside, allowing GITM's winds to accelerate due to the day-to-night pressure gradient.

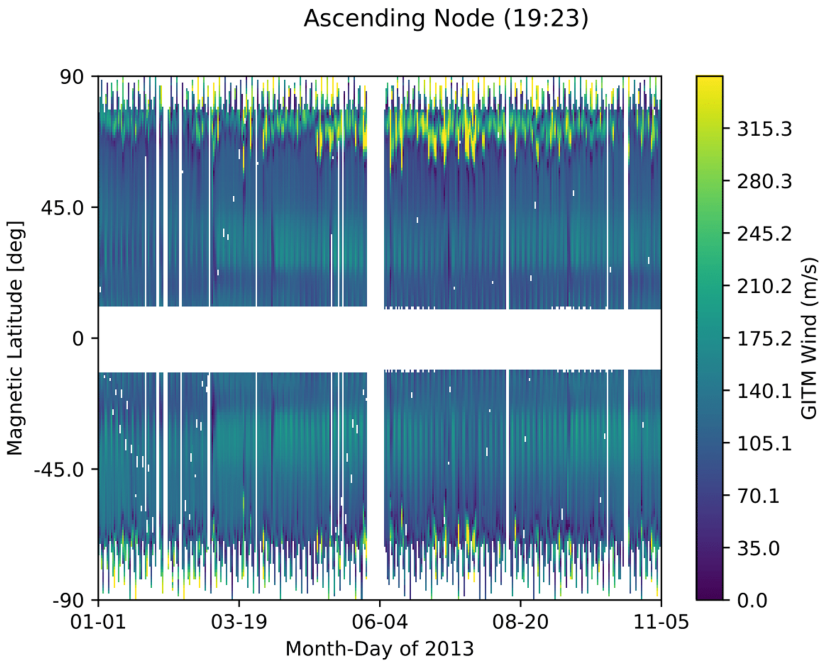
Exploring V_x specifically during the middle 10 days of March (Figure 5) shows the differences between the GITM results and GOCE winds in greater detail (as is done in Figure 1, but in Apex coordinates). GITM shows diurnal variability of V_x, as GOCE does, but GITM shows higher winds speeds in bands at $\sim \pm 20°$ magnetic latitude, most likely due to reduced ion drag, as described above. GITM's wind speeds are more similar to GOCE at high latitudes in the dusk sector, but GOCE wind speeds are significantly larger in the southern auroral zone in the dawn sector.

GOCE V_x probability distributions were compared to their GITM counterparts in each of three latitude ranges for three AE bins (Figure 6). GITM's probability distributions were generally narrower than those of GOCE outside of the polar region, most drastically in the mid-latitudes, which may be related to GITM's modeling of the ion drag. The stronger signature of diurnal variability in the GOCE data additionally shows up as wider spread in the distribution. Even though GITM's distributions were narrower in the mid-latitudes, its values of mean V_x were closer to those of GOCE than in the auroral zone. GITM's peak probabilities skewed towards larger V_x in comparison to GOCE in the mid-latitudes, where it showed a tendency to overestimate wind speed, but skewed towards smaller V_x than GOCE in the auroral latitudes (with the exception of high activity), where it underestimated wind speeds. GITM's probabilities matched GOCE's quite well in the polar region, with the exception of during high activity, where it tended to overestimate the wind speed.

This article is protected by copyright. All rights reserved.

Author Manuscript

(a) GITM wind speeds near dusk



(b) GOCE wind speeds near dusk

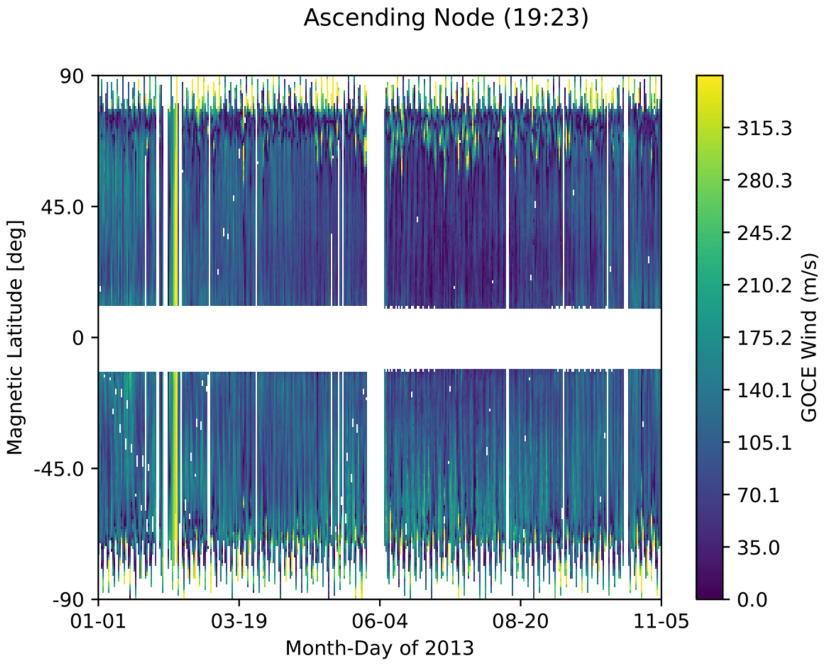
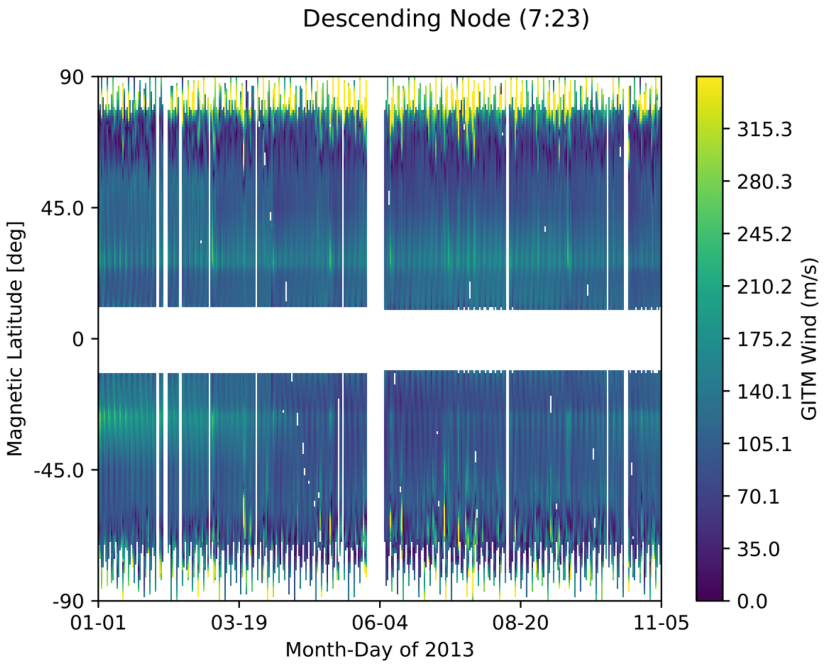


Figure 2. Time series and latitude plots of the (a) GITM and (b) GOCE horizontal wind speed for the ascending node for Jan. 1 - Nov. 5, 2013.

This article is protected by copyright. All rights reserved.

Author Manuscript

(a) GITM wind speeds near dawn



(b) GOCE wind speeds near dawn

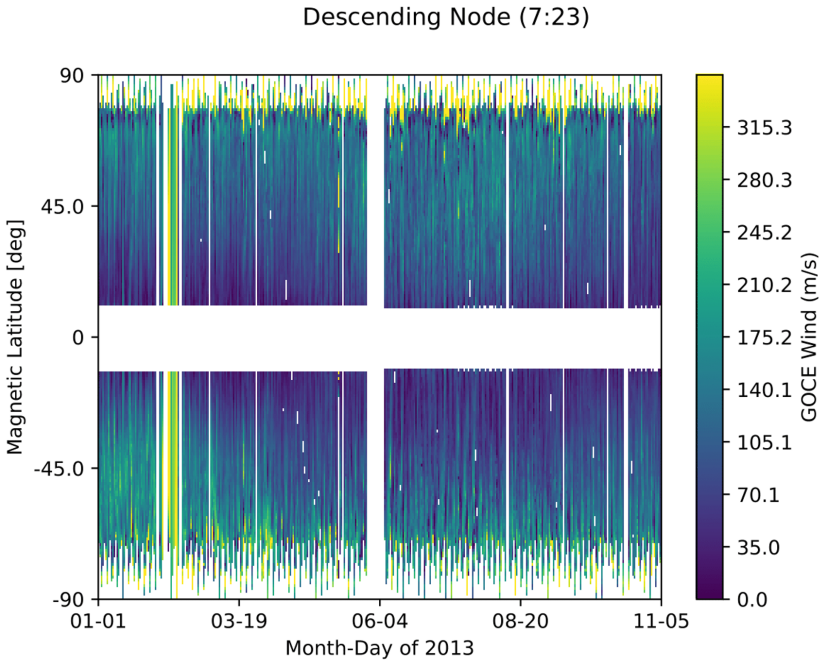


Figure 3. (a) Time series and latitude plots of the (a) GITM and (b) GOCE horizontal wind speed for the descending node for Jan. 1 - Nov. 5, 2013.

This article is protected by copyright. All rights reserved.

Author Manuscript

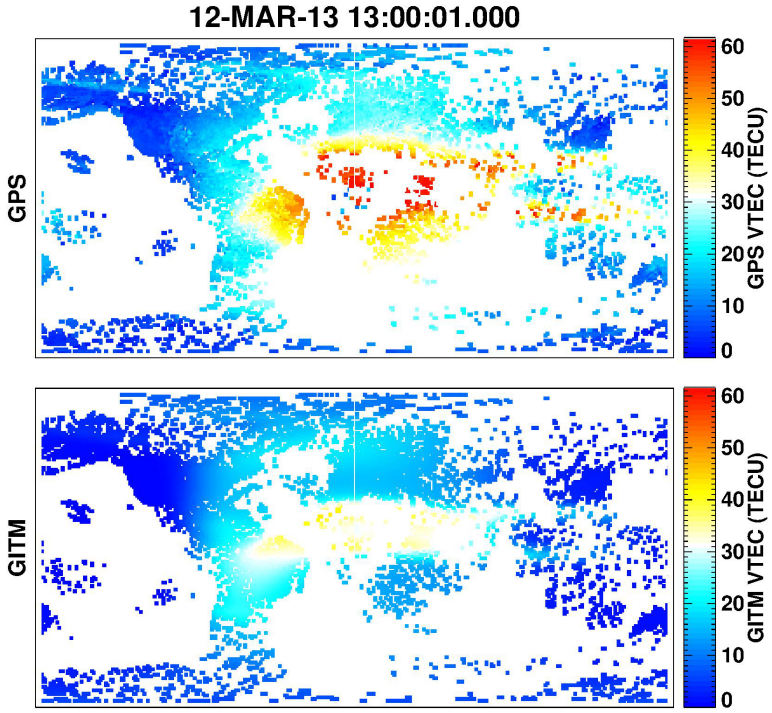


Figure 4. Global measurements (top) and GITM results (bottom) of the vertical total electron content at 13 UT on March 12, 2013. The plot is in latitude/longitude geographic coordinates.

The 10-month window chosen for this study allowed us to explore how different conditions affected the GITM results. Specifically, AE, MLT, Day of Year (DOY), and F10.7 were investigated. Because GITM was sampled at the GOCE locations and times, the number of counts of V_x per bin of the selected parameter were identical for both sets of data. The Northern and Southern Hemisphere data were combined for this analysis, except when binning the data as a function of MLT.

Figure 7 displays the dependence of V_x on the AE index for GITM in comparison to GOCE. The GOCE data show that in the low- and mid-latitudes, thermospheric horizontal wind speeds decrease slightly for increasing activity level. In both these regions, GITM overestimated the wind speed, with the magnitude of the overestimation generally growing as activity level increased. GITM's wind speed overestimation was most clear in the low-latitudes, where it grew from ∼5 m/s to ∼30 m/s from AE values of 50 to 1200. In contrast to the mid-latitudes, where GITM's V_x values slightly decreased with activity, in the low-latitudes, GITM's V_x slightly increased with activity. In the auroral and polar zones, GITM performed much better in capturing the characteristic increase in V_x with activity level shown in the GOCE data, even though it began to overestimate the wind speed above AE=400 in both cases, growing to a difference of at least ∼80 m/s at AE=1200.

Next, we consider variations with magnetic local time (Figure 8), noting characteristic troughs in the data around 7 and 19 hours, due to GOCE being in a roughly dusk-to-dawn orbit (in geographic coordinates).

Due to the offset between the geographic and magnetic poles, GOCE was able to sample all MLTs in the polar cap, but only near dawn and dusk at lower latitudes. In

This article is protected by copyright. All rights reserved.

Author Manuscript

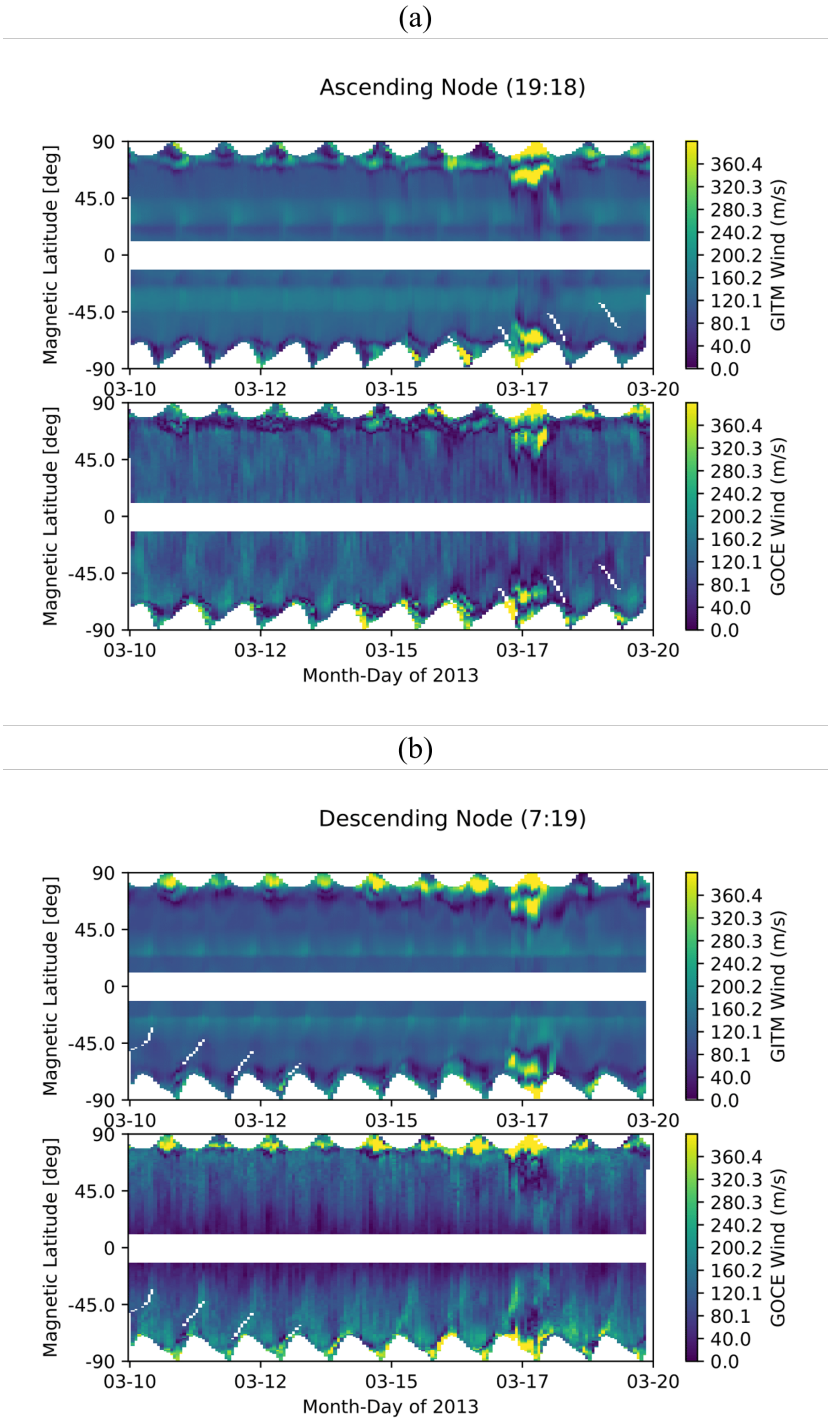


Figure 5. Time series and latitude plots of the GITM and GOCE horizontal wind for the ascending node (top) and descending node (bottom) between March 10 and March 20. GITM sufficiently captures the diurnal variability shown in the GOCE data but overestimates horizontal wind speed at $\sim \pm 20^{\circ}$ MLAT.

This article is protected by copyright. All rights reserved.

Author Manuscript

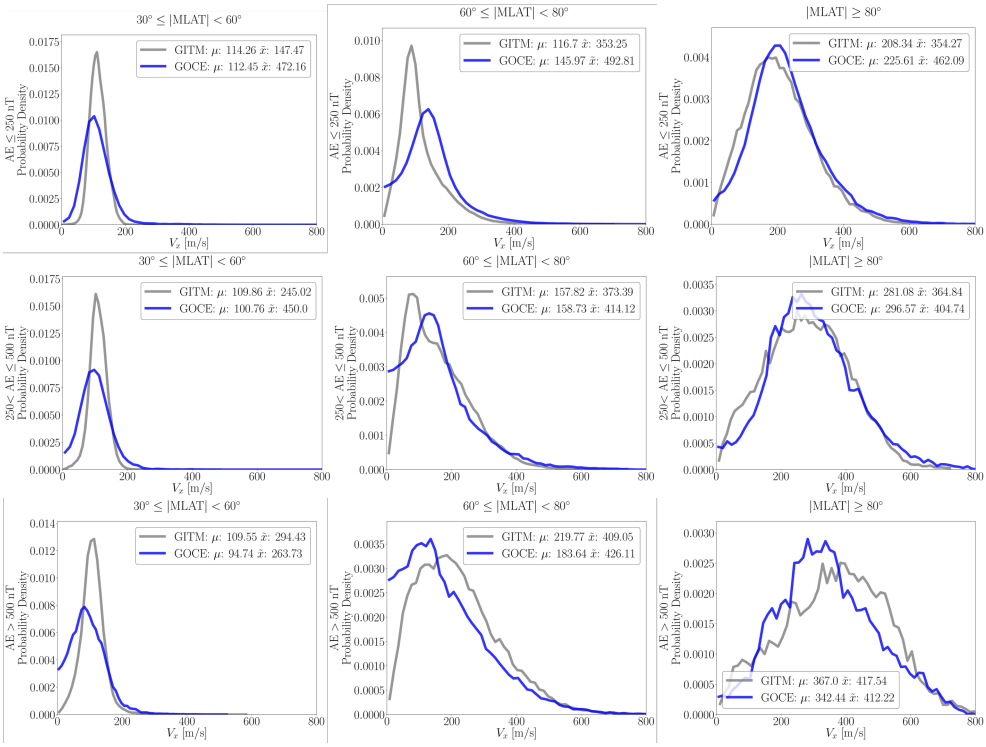


Figure 6. Probability densities of V_x for GOCE compared to GITM across the three MLAT ranges (from left to right: Mid-, auroral-, and polar-latitudes), for three different levels of geomagnetic activity described by the AE index (from top to bottom: AE $\leq$ 250, 250 $<$ AE $\leq$ 500, and AE $>$ 500). GITM's performance tended to increase with magnetic latitude and activity level. In the legend of each plot, μ is the mean and $\tilde{x}$ is the median.

the northern auroral zone, GOCE MLT coverage was limited between mid-morning to evening, while in the southern auroral zone, GOCE covered all MLTs but excluded those around noon. GITMs V_x values exceeded those of GOCE more often when V_x for both was distributed by AE. When V_x was distributed by MLT, however, GITMs V_x values were more often lesser than those of GOCE. GITM best matched GOCE in the mid-latitudes, for which GITM's mean V_x was generally consistent with GOCE's, although with significant variability. The mismatch between GITM and GOCE was strongest in both auroral zones, with the GITM mean V_x exceeding GOCE only for 13$\leq$MLT$\leq$17. In the auroral zones, the greatest underestimation by GITM occurred at MLT$\approx$0 and MLT$\approx$7 in the southern hemisphere, where GITM's mean V_x undershot GOCE V_x by nearly 100 m/s, approximately the same magnitude by which GITM overestimated the mean V_x in the northern hemisphere near MLT=15. In the polar zone, GITM performed best for 7$\leq$MLT$\leq$15, where it's 25th, 50th (median), and 75th percentiles of V_x tracked GOCE with minimal deviation. Outside of that MLT range, GITM generally underestimated V_x by $\sim$50 m/s. Overall, GITM demonstrates the best performance on the dayside, and the worst performance on the nightside around midnight MLT. It may be that the solar-driven ionization, and therefore the ion drag, may be best modeled at high latitudes on the dayside.

We also compared seasonal effects in V_x separately for each hemisphere (Figure 9). Due to the reentry of GOCE in November of 2013, we were unable to extend this analysis through December of 2013. The GOCE data showed differing patterns depending on the latitude ranges considered. In the northern polar zone, GOCE showed no discernible

This article is protected by copyright. All rights reserved.

Author Manuscript

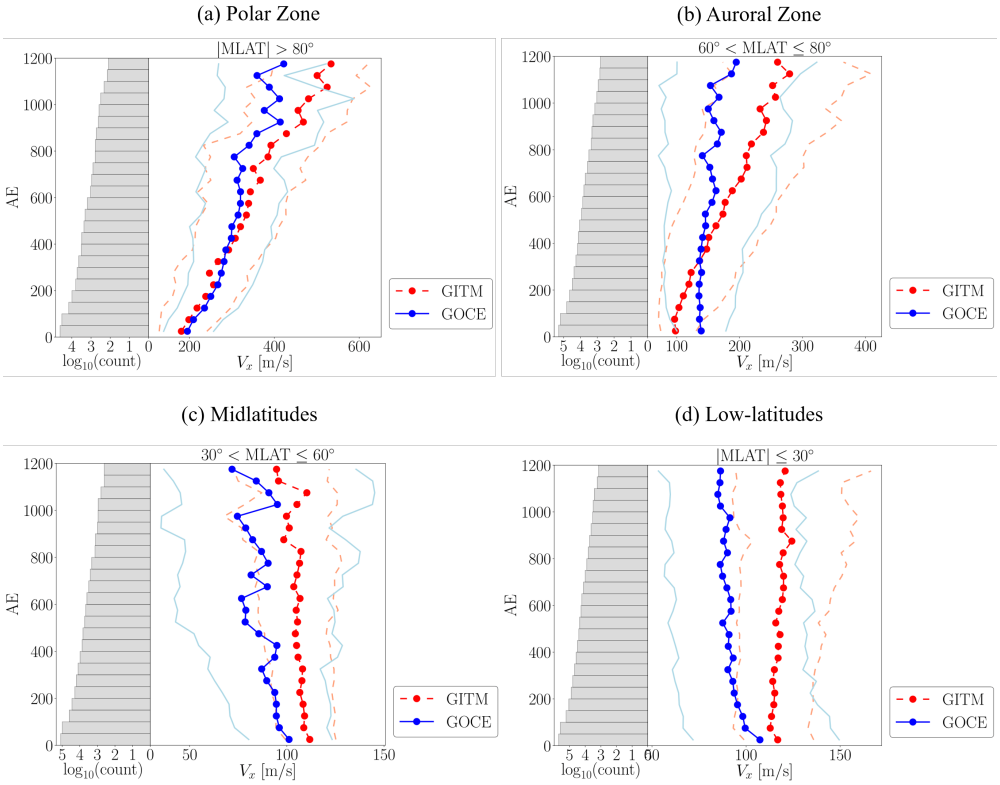


Figure 7. The 25th, 50th, and 75th percentiles of V_x per bin of AE for both the GITM and GOCE data constructing an adjacent histogram of the number of counts of data per bin. Lines corresponding to GITM are red and dashed, and lines corresponding to GOCE are blue and solid. The 25th and 75th percentiles of the GITM V_x values are in light blue, while the 50th percentile is in rich blue, marked with circles, while the 25th and 75th percentiles of the GOCE V_x values are in light red, while the 50th percentile is in rich red, also topped with circles. In the top row from left to right, the results are shown for the polar latitudes and then auroral latitudes, and in the bottom row from left to right, the results are shown for mid-latitudes and the equatorial region.

seasonal dependence, with its values of mean V_x oscillating around ∼250 m/s throughout the entire time considered. GITM's values of mean V_x tracked those of GOCE very well in this region, with GITM slightly overestimating the wind speed in the days surrounding the summer solstice. GITM's 25th and 75th percentile V_x values also did not deviate much at all from those of GOCE. Contrary to the northern case, in the southern polar zone, GITM underestimated V_x in all percentiles, even though it was able to capture the overall trend in the wind speeds throughout the year. Similar to how GITM overestimated the wind most in the northern polar zone during the summer solstice, it is around that time (i.e. the southern winter solstice) that GITM underestimated the wind the southern polar zone most significantly.

In the northern auroral zone, the GOCE data showed no discernible dependency on season, with its mean V_x clustered around ∼120 m/s throughout the year. GITM reproduced this behavior overall, with the slight caveat of underestimating the winds by up to ∼ 30 m/s between January and late February (i.e. the northern winter). GITM's 25th percentile V_x values were similarly close to those of GOCE, but GITM's 75th per-

This article is protected by copyright. All rights reserved.

Author Manuscript

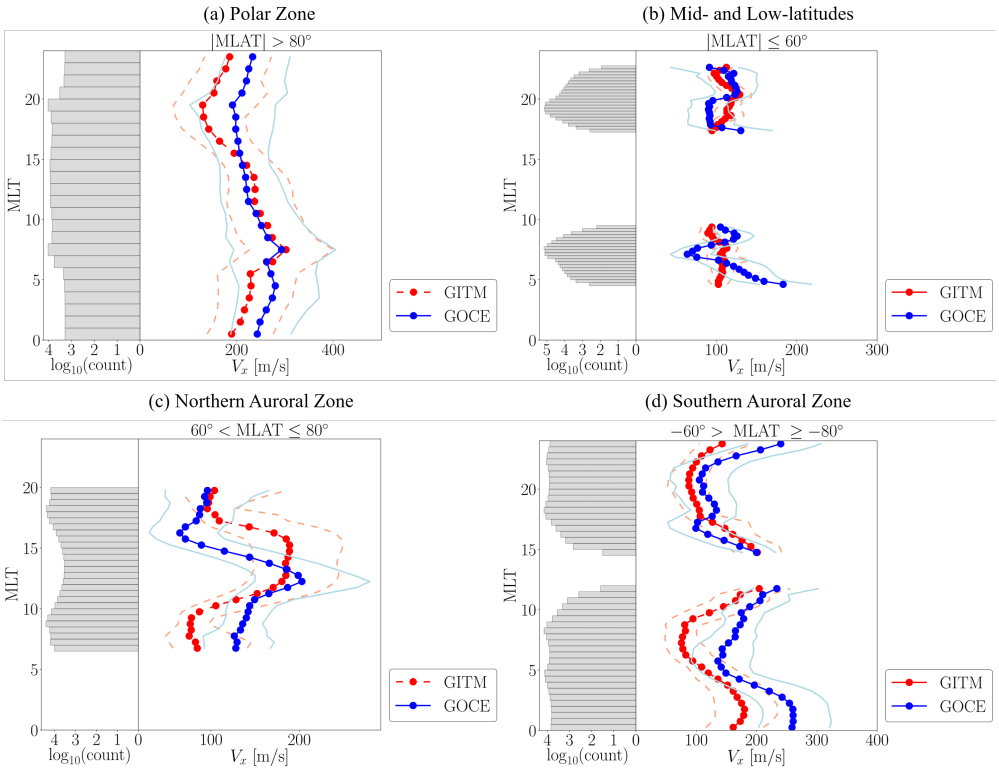


Figure 8. Top row, left to right: Percentiles (25th, 50th, and 75th) of V_x and data count, per bin of MLT over the polar region (bin width of 1 hr), auroral latitudes, and low and middle latitudes (bin width of 15 minutes). Bottom row, left to right: Percentiles (25th, 50th, and 75th) of V_x and data count, per bin of MLT index over the Northern auroral oval and Southern auroral oval, with bin widths of 30 min for both.

centile V_x values were much higher than GOCE's between the March Equinox and just before the autumnal equinox, indicating that GITM's horizontal winds were too variable during the summer. In the southern auroral zone, the GOCE wind speeds were nearly identical to that of the northern auroral zone, except that the values of V_x were higher by tens of m/s. Here, GITM underestimated V_x in all percentiles throughout the entire time shown, and did not capture the contour of the GOCE data, instead showing a slight decline in winds speed that reached a nadir at ∼100 m/s during the southern winter solstice before increasing again. GITM's underestimation can be highlighted by noting that its 75th percentile V_x values tracked the best with GOCE's mean V_x values throughout the entire year, and that its mean V_x values tracked best with GOCE's 25th percentile V_x values.

In the mid- and low-latitudes, for both hemispheres, the GOCE data showed a slight slowing of the wind across all percentiles that reached its nadir around June, before increasing slightly again. GOCE's mean V_x values clustered around 100 m/s in January for both hemispheres and decreased to ∼80 m/s by the summer solstice, but the following increase in wind speed leading up to the autumnal equinox was slightly more prominent in the southern hemisphere by several m/s. GITM was closest to GOCE during early January. During the rest of the year, it overestimated V_x in all percentiles compared to GOCE in both hemispheres, and its performance was less laudable in the northern hemisphere than the southern hemisphere. In the northern hemisphere, GITM did not capture the seasonal trend in V_x featuring the trough during the summer solstice, and its

This article is protected by copyright. All rights reserved.

Author Manuscript

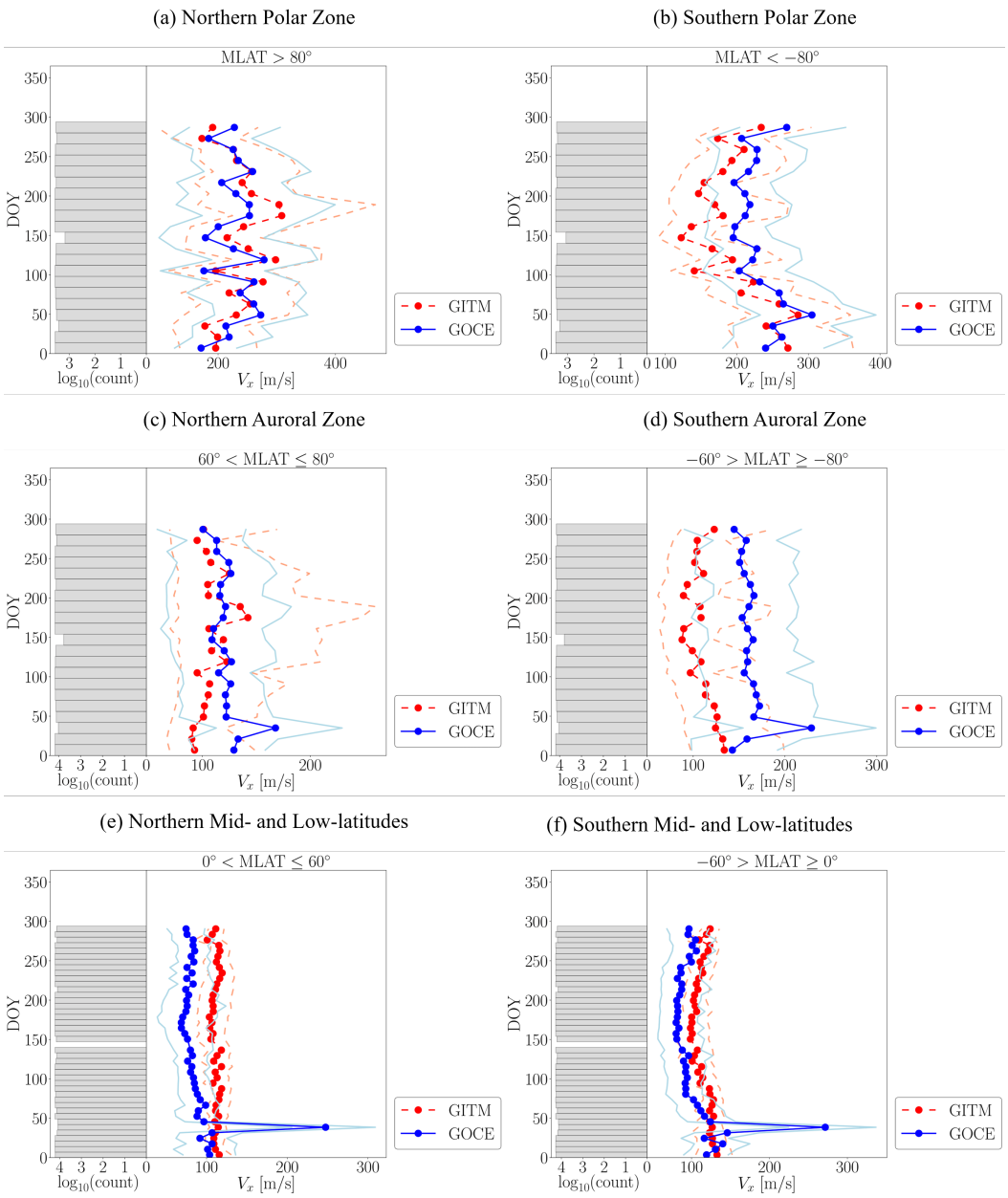


Figure 9. From the top down: Percentiles (25th, 50th, and 75th) of V_x and data count, per bin of DOY index over the Northern Hemisphere (left column) and Southern Hemisphere (right column), the polar cap an auroral oval (bin width 2 weeks), and middle latitudes (bin width 1 week). The high wind speeds in the GOCE data in mid February correspond to the bright yellow regions in Figures **??** and **??**, where GOCE measured anomalously high wind speeds. The associated error with those measurements did not warrant their exclusion, despite their anomalous nature.

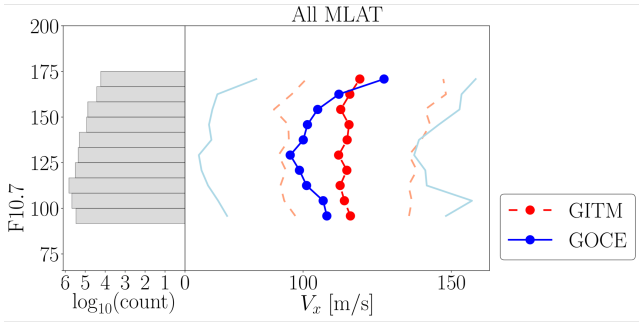
mean V_x values remained close to ∼100 m/s during the entire year. GITM performed better in the southern hemisphere, capturing the seasonality in V_x throughout the entire time shown, with its mean V_x values differing from those of GOCE by $\sim 10 - 15$ m/s outside of January and February.

This article is protected by copyright. All rights reserved.

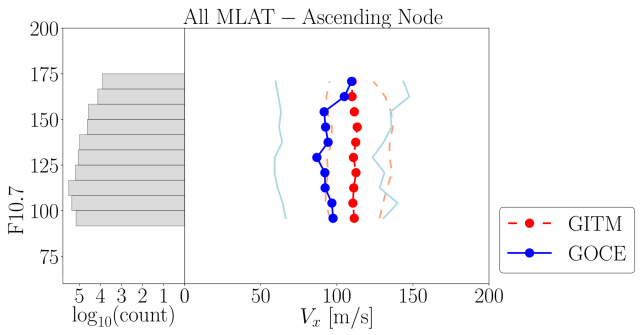
Author Manuscript

We next compare the horizontal wind response to the F10.7 flux between GITM and GOCE across all latitudes (Figure 10). For the available range of F10.7 between ∼87 sfu and ∼175, the GOCE wind speed for both dusk and dawn combined (a) decreased in mean V_x down from ∼110 m/s around 90 sfu to ∼100 m/s around 130 sfu, before increasing to ∼140 m/s at 175 sfu. The GITM results did not capture this trend, with the mean V_x remaining around ∼120 m/s throughout the entire F10.7 range. Both GITM's 25th and 75th percentile V_x values were constrained between GOCE's 25th and 75th percentile values throughout the entire F10.7 range, indicating that GITM's modeled winds were insufficiently variable with respect to the GOCE measurements.

(a) Dependence on F10.7, all Local Times



(b) Dependence on F10.7, Dusk Sector



(c) Dependence on F10.7, Dawn Sector

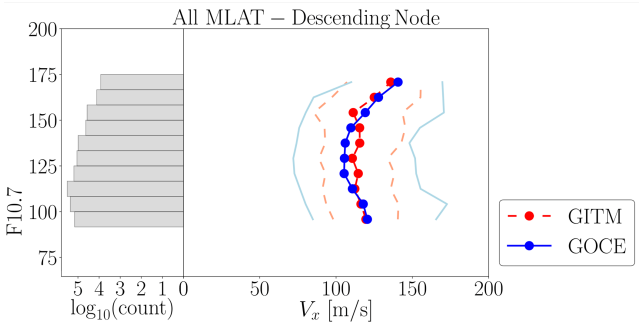


Figure 10. Percentiles (25th, 50th, and 75th) of V_x and data count, per bin of F10.7 flux, over the full MLAT range, for: (a) both dusk and dawn combined; (b) dusk sector only; and (c) dawn sector only.

When V_x between GITM and GOCE is compared for the ascending (b, dusk) and descending (c, dawn) nodes separately, some important differences are noticeable. For

This article is protected by copyright. All rights reserved.

Author Manuscript

dusk (Figure 10b), GITM mean V_x was consistently higher than GOCE mean V_x throughout the entire range of F10.7, except at the highest levels. GITM also did not accurately capture the slower wind speeds seen in the data, as shown by its 25th percentile values being greater than those of GITM by ~ 30 m/s. This behavior was not seen, however, for the 75th percentiles, for which GITM matched GOCE very well. GITM matched GOCE better for dawn (descending node) (Figure 10c), following its behavior of decreasing from 90<F10.7≤135, and rising from 135<F10.7≤175. GITM mean V_x matched GOCE very well throughout the entire range of F10.7, while its 25th percentile values were slightly lower than those of GOCE, and its 75th percentile values were slightly higher than those of GOCE.

4 Conclusion and Discussion

Overall, GITM demonstrated satisfactory capability in modeling the horizontal thermospheric wind in comparison to GOCE, but also shows areas for improvement. The major results are as follows:

1. The directionality of GITM's wind speed was mostly in qualitative agreement with GOCE in the east component of the horizontal cross-track wind at all latitudes and the north component at higher latitudes.
2. Probability distributions for GITM and GOCE V_x show that GITM's performance improved as a function of MLAT, being best in the polar zone, and worst in the midlatitudes, where it seemed to have a persistent jet possibly related to too weak of ion drag.
3. As a function of geomagnetic activity represented by AE, GITM again performed the best in the polar and auroral zones, but overestimated horizontal winds for AE≥400. Outside of the polar and auroral regions, GITM V_x consistently exceeded that of GOCE at all levels of AE.
4. As a function of MLT, GITM performed the best in the polar zone near noon and worst in the auroral zones near midnight. When GITM was inaccurate compared to GOCE as a function of MLT, its tendency was to underestimate V_x more often than overestimate, with this occurring prominently for 12 >MLT< 17.
5. As a function of DOY (season), GITM performed best in the northern polar and auroral zones, and worst in the southern auroral and polar zones. Seasonality in the mid- and low-latitudes was best captured by GITM in the southern hemisphere. GITM primarily underestimated horizontal winds in the winter and overestimated them in the summer, although the amount of over and underestimation varied.
6. As a function of F10.7, GITM displayed less variability than GOCE, and overall slightly overestimated horizontal winds, except for F10.7>$\sim$ 150, where it tracked GOCE the best.
7. GITM's underestimation of winds in the summer could be an indication that ion drag could be inaccurate, which may be driven by either electron densities that are inaccurate or ion drifts that are inaccurate. This is true especially in the mid-latitudes, where there is a persistent larger wind modeled by GITM than was observed by GOCE.

This study indicates that GITM's modeling of the cross-track (horizontal) wind speed is overall best at higher magnetic latitudes, and characterized by overestimation in the mid- and low-latitudes. At higher activities and higher latitudes, this overestimation persists. This may be due to strong driving by the (Weimer, 2005) model, with a lack of variability within the drivers that has been described by other research (Cousins & Shepherd, 2012).

Addressing the concerns described in this study may improve GITM's ability to capture seasonality, especially at the mid- and low-latitudes. Additional work includes

This article is protected by copyright. All rights reserved.

Author Manuscript

extending the analysis to investigating how improved modeling of viscosity, ion drag, and temperature can aid in GITM's modeling of thermospheric horizontal winds, as well as a follow-up study covering a wider period of time and incorporating both data from satellites and ground-based FPIs. It is additionally important to investigate the role of lower atmosphere drivers for increasing GITM's accuracy. A similar analysis will be extended to vertical winds in order to investigate the underlying mechanisms that are primarily responsible for driving them at various latitudes and driving conditions.

Acknowledgments

This work was supported by the joint NSF-NASA Space Weather with Quantified Uncertainties program under NASA grant: 80NSSC20K1581. We additionally acknowledge use of the World Data Center for Geomagnetism to obtain AE Index measurements for the year of 2013 (http://wdc.kugi.kyoto-u.ac.jp/dstae/index.html). Data for the GOCE mission are available at: https://doi.org/10.5270/esa-l8g67jw.
GOCE is part of the ESA Living Planet Program:
https://www.esa.int/Applications/Observing_the_Earth/GOCE.
The selected data and code used for this study is housed on the DeepBlue archive of the University of Michigan: https://doi.org/10.7302/wzc1-vc88.

References

Billett, D. D., McWilliams, K. A., & Conde, M. G. (2020). Colocated observations of the e and f region thermosphere during a substorm. *Journal of Geophysical Research: Space Physics*, *125*(11), e2020JA028165. doi: https://doi.org/10.1029/2020JA028165

Biondi, M. A. (1984). Measured vertical motion and converging and diverging horizontal flow of the midlatitude thermosphere. *Geophysical Research Letters*, *11*, 8487.

Biondi, M. A., & Sipler, D. P. (1985). Horizontal and vertical winds and temperatures in the equatorial thermosphere: Measurements from natal, brazil during augustseptember 1982. *Planetary and Space Science*, *33*(7), 817-823. doi: https://doi.org/10.1016/0032-0633(85)90035-2

Bowman, M. R., Gibson, A. J., & Sandford, M. C. W. (1969). Atmospheric sodium measured by a tuned laser radar. *Nature*, *221*(5179), 456-457. doi: 10.1038/221456a0

Burns, A. G., Killeen, T. L., & Roble, R. G. (1989). Causes of changes in composition calculated using a thermospheric general circulation model. *J. Geophys. Res.*, *94*, 36703686.

Burns, A. G., Killeen, T. L., & Roble, R. G. (1991). A simulation of the thermospheric composition changes during an impulse storm. *J. Geophys. Res.*, *96*, 1415314167.

Cai, L., Oyama, S., Aikio, A., Vanhamki, H., & Virtanen, I. (2019). Fabry-perot interferometer observations of thermospheric horizontal winds during magnetospheric substorms. *Journal of Geophysical Research: Space Physics*, *124*(5), 3709-3728. doi: https://doi.org/10.1029/2018JA026241

Ceplecha, Z., Borovička, J., Elford, W. G., ReVelle, D. O., Hawkes, R. L., Porubčan, V., & Šimek, M. (1998). Meteor phenomena and bodies. *Space Science Reviews*, *84*(3), 327-471. doi: 10.1023/A:1005069928850

Chamberlin, P. C., Woods, T. N., & Eparvier, F. G. (2007). Flare irradiance spectral model (fism): Daily component algorithms and results. *Space Weather*, *5*(7). doi: https://doi.org/10.1029/2007SW000316

Chamberlin, P. C., Woods, T. N., & Eparvier, F. G. (2008). Flare irradiance spectral model (fism): Flare component algorithms and results. *Space Weather*, *6*(5). doi: https://doi.org/10.1029/2007SW000372

This article is protected by copyright. All rights reserved.

Author Manuscript

Chau, J. L., & Clahsen, M. (2019). Empirical phase calibration for multistatic specular meteor radars using a beamforming approach. *Radio Science*, *54*(1), 60-71. doi: https://doi.org/10.1029/2018RS006741

Chu, X., Yu, Z., Gardner, C. S., Chen, C., & Fong, W. (2011). Lidar observations of neutral fe layers and fast gravity waves in the thermosphere (110155 km) at mcmurdo (77.8°s, 166.7°e), antarctica. *Geophysical Research Letters*, *38*(23). doi: https://doi.org/10.1029/2011GL050016

Conde, M., & Smith, R. W. (1998). Spatial structure in the thermospheric horizontal wind above poker flat, alaska, during solar minimum. *Journal of Geophysical Research: Space Physics*, *103*(A5), 9449-9471. doi: https://doi.org/10.1029/97JA03331

Cousins, E. D. P., & Shepherd, S. G. (2012). Statistical maps of small-scale electric field variability in the high-latitude ionosphere. *J. Geophys. Res.*, *117*, 12304. doi: 10.1029/2012JA017929

Dandenault, P. B. (2018). Mentat: A new wind model for earth's thermosphere. *Journal of Geophysical Research: Space Physics*, *123*(8), 7124-7147. doi: https://doi.org/10.1029/2018JA025551

Davis, T. N., & Sugiura, M. (1966). Auroral electrojet activity index ae and its universal time variations. *Journal of Geophysical Research (1896-1977)*, *71*(3), 785-801. doi: https://doi.org/10.1029/JZ071i003p00785

Dhadly, M. S., Emmert, J. T., Drob, D. P., Conde, M. G., Aruliah, A., Doornbos, E., ... Ridley, A. J. (2019). Hl-twim empirical model of high-latitude upper thermospheric winds. *Journal of Geophysical Research: Space Physics*, *124*(12), 10592-10618. doi: https://doi.org/10.1029/2019JA027188

Doornbos, E. (2011). Thermospheric density and wind determination from satellite dynamics (ph.d. thesis). *Delft University of Technology, Delft, The Netherlands*.

Doornbos, E., van den IJssel, J., Luhr, H., Forster, M., & Koppenwallner, G. (2010). Neutral density and crosswind determination from arbitrarily oriented multiaxis accelerometers on satellites. *Journal of Spacecraft and Rockets*, *47*(4), 580-589. doi: 10.2514/1.48114

Drob, D. P., Emmert, J. T., Crowley, G., Picone, J. M., Shepherd, G. G., Skinner, W., ... Vincent, R. A. (2008). An empirical model of the earth's horizontal wind fields: Hwm07. *Journal of Geophysical Research: Space Physics*, *113*(A12). doi: https://doi.org/10.1029/2008JA013668

Drob, D. P., Emmert, J. T., Meriwether, J. W., Makela, J. J., Doornbos, E., Conde, M., ... Klenzing, J. H. (2015). An update to the horizontal wind model (hwm): The quiet time thermosphere. *Earth and Space Science*, *2*, 301-319.

fang Du, L., tao Yang, G., hong Wang, J., Yue, C., & xiang Chen, L. (2017). Implementing a wind measurement doppler lidar based on a molecular iodine filter to monitor the atmospheric wind field over beijing. *Journal of Quantitative Spectroscopy and Radiative Transfer*, *188*, 3-11. (Advances in Atmospheric Light Scattering: Theory and Remote Sensing Techniques) doi: https://doi.org/10.1016/j.jqsrt.2016.07.013

Floberghagen, R., Fehringer, M., Lamarre, D., Muzi, D., Frommknecht, B., Steiger, C., ... da Costa, A. (2011). Mission design, operation and exploitation of the gravity field and steady-state ocean circulation explorer mission. *Journal of Geodesy*, *85*, 749-758. doi: https://doi.org/10.007/s00190-011-0498-3

Fujii, J., Nakamura, T., Tsuda, T., & Shiokawa, K. (2004). Comparison of winds measured by mu radar and fabryperot interferometer and effect of oi5577 airglow height variations. *Journal of Atmospheric and Solar-Terrestrial Physics*, *66*(6), 573-583. (Dynamics and Chemistry of the MLT Region - PSMOS 2002 International Symposium) doi: https://doi.org/10.1016/j.jastp.2004.01.010

Fuller-Rowell, T. J., & Evans, D. S. (1987). Height-integrated pedersen and hall conductivity patterns inferred from the tiros-noaa satellite data. *Journal of Geo-*

This article is protected by copyright. All rights reserved.

Author Manuscript

physical Research: Space Physics, *92*(A7), 7606-7618. doi: https://doi.org/10.1029/JA092iA07p07606

Gao, Q., Chu, X., Xue, X., Dou, X., Chen, T., & Chen, J. (2015). Lidar observations of thermospheric na layers up to 170 km with a descending tidal phase at lijiang (26.7°n, 100.0°e), china. *Journal of Geophysical Research: Space Physics*, *120*(10), 9213-9220. doi: https://doi.org/10.1002/2015JA021808

Gardner, J., Broadfoot, A., McNeil, W., Lai, S., & Murad, E. (1999). Analysis and modeling of the glo-1 observations of meteoric metals in the thermosphere. *Journal of Atmospheric and Solar-Terrestrial Physics*, *61*(7), 545-562. doi: https://doi.org/10.1016/S1364-6826(99)00013-9

Gasperini, F., Forbes, J. M., Doornbos, E. N., & Bruinsma, S. L. (2015). Wave coupling between the lower and middle thermosphere as viewed from timed and goce. *Journal of Geophysical Research: Space Physics*, *120*(7), 5788-5804. doi: https://doi.org/10.1002/2015JA021300

Gasperini, F., Forbes, J. M., Doornbos, E. N., & Bruinsma, S. L. (2016). Synthetic thermosphere winds based on champ neutral and plasma density measurements. *Journal of Geophysical Research: Space Physics*, *121*(4), 3699-3721. doi: https://doi.org/10.1002/2016JA022392

Guo, J.-P., Deng, Y., Zhang, D.-H., Lu, Y., Sheng, C., & Zhang, S.-R. (2018). The effect of subauroral polarization streams on ionosphere and thermosphere during the 2015 st. patrick's day storm: Global ionosphere-thermosphere model simulations. *Journal of Geophysical Research: Space Physics*, *123*(3), 2241-2256. doi: https://doi.org/10.1002/2017JA024781

Harding, B. J., Ridley, A. J., & Makela, J. J. (2019). Thermospheric weather as observed by ground-based fpis and modeled by gitm. *Journal of Geophysical Research: Space Physics*, *124*(2), 1307-1316. doi: https://doi.org/10.1029/2018JA026032

Hedin, A. E., Biondi, M. A., Burnside, R. G., Hernandez, G., Johnson, R. M., Killeen, T. L., ... Virdi, T. S. (1991). Revised global model of thermosphere winds using satellite and ground-based observations. *Journal of Geophysical Research: Space Physics*, *96*(A5), 7657-7688. doi: https://doi.org/10.1029/91JA00251

Hedin, A. E., Spencer, N. W., & Killeen, T. L. (1988). Empirical global model of upper thermosphere winds based on atmosphere and dynamics explorer satellite data. *Journal of Geophysical Research: Space Physics*, *93*(A9), 9959-9978. doi: https://doi.org/10.1029/JA093iA09p09959

Helmboldt, J. F., & Taylor, G. B. (2020). All-sky tracking of sporadic field-aligned irregularities as a novel probe of thermospheric winds. *Earth and Space Science*, *7*(4), e2019EA000867. doi: https://doi.org/10.1029/2019EA000867

Hsu, V. W., Thayer, J. P., Lei, J., & Wang, W. (2014). Formation of the equatorial thermosphere anomaly trough: Local time and solar cycle variations. *J. Geophys. Res.: Sp. Phys.*, *119*.

Innis, J. L., & Conde, M. (2002). High-latitude thermospheric vertical wind activity from dynamics explorer 2 wind and temperature spectrometer observations: Indications of a source region for polar cap gravity waves. *J. Geophys. Res.: Sp. Phys.*, *107*, 1172.

Jiang, G., Xu, J., Wang, W., Yuan, W., Zhang, S., Yu, T., ... Li, Q. (2018). A comparison of quiet time thermospheric winds between fpi observations and model calculations. *Journal of Geophysical Research: Space Physics*, *123*(9), 7789-7805. doi: https://doi.org/10.1029/2018JA025424

Johnson, F. S., Hanson, W. B., Coley, W. R., Carignan, G. R., & Spencer, N. W. (1995). Gravity waves near 300 km over the polar cap. *J. Geophys. Res.*, *100*(23), 23,99324,002.

Khattatov, B. V., Yubin, V. A., Geller, M. A., Hays, P. B., & Vincent, R. A. (1997). Diurnal migrating tide as seen by the high-resolution doppler imager/uars:

This article is protected by copyright. All rights reserved.

Author Manuscript

1. monthly mean global meridional winds. *Journal of Geophysical Research: Atmospheres*, *102*(D4), 4405-4422. doi: https://doi.org/10.1029/96JD03655

Killeen, T. L., Nardi, B., Purcell, P. N., Roble, R. G., Fuller-Rowell, T. J., & Rees, D. (1992). *Geophysical Research Letter*, *19*(11), 1093-1096.

Killeen, T. L., Wu, Q., Solomon, S. C., Ortland, D. A., Skinner, W. R., Niciejewski, R. J., & Gell, D. A. (2006). Timed doppler interferometer: Overview and recent results. *Journal of Geophysical Research: Space Physics*, *111*(A10). doi: https://doi.org/10.1029/2005JA011484

Korotyshkin, D., Merzlyakov, E., Sherstyukov, O., & Valiullin, F. (2019). Mesosphere/lower thermosphere wind regime parameters using a newly installed skiymet meteor radar at kazan (56°n, 49°e). *Advances in Space Research*, *63*(7), 2132-2143. doi: https://doi.org/10.1016/j.asr.2018.12.032

Liu, A. Z., Guo, Y., Vargas, F., & Swenson, G. R. (2016). First measurement of horizontal wind and temperature in the lower thermosphere (105140km) with a na lidar at andes lidar observatory. *Geophysical Research Letters*, *43*(6), 2374-2380. doi: https://doi.org/10.1002/2016GL068461

Liu, H., Doornbos, E., & Nakashima, J. (2016). Thermospheric wind observed by goce: Wind jets and seasonal variations. *Journal of Geophysical Research: Space Physics*, *121*(7), 6901-6913. doi: https://doi.org/10.1002/2016JA022938

Liuzzo, L. R., Ridley, A. J., Perlongo, N. J., Mitchell, E. J., Conde, M., Hampton, D. L., ... Nicolls, M. J. (2015). High-latitude ionospheric drivers and their effects on wind patterns in the thermosphere. *J. Geophys. Res.: Sp. Phys.*, *120*, 715735.

Makela, J., Meriwether, J. W., Ridley, A. J., Ciocca, M., & Castellez, M. W. (2012). Large-scale measurements of thermospheric dynamics with a multisite fabry-perot interferometer network: Overview of plans and results from midlatitude measurements. *International Journal of Geophysics*, *2012*. doi: https://doi.org/10.1155/2012/872140

Makela, J. J., Fisher, D. J., Meriwether, J. W., Buriti, R. A., & Medeiros, A. F. (2013). Near-continual ground-based nighttime observations of thermospheric neutral winds and temperatures over equatorial brazil from 2009 to 2012. *Journal of Atmospheric and Solar-Terrestrial Physics*, *103*, 94-102.

Martinis, C., Meriwether, J., Niciejewski, R., Biondi, M. A., Fesen, C., & Mendillo, M. (2001). Zonal neutral winds at equatorial and low latitudes. *Journal of Atmospheric and Solar-Terrestrial Physics*, *63*, 1559-1569.

Meriwether, J. W., Makela, J. J., Huang, Y., Fisher, D. J., Buriti, R. A., Medeiros, A. F., & Takahashi, H. (2011). Climatology of the nighttime equatorial thermospheric winds and temperatures over brazil near solar minimum. *Journal of Geophysical Research: Space Physics*, *116*(A4). doi: https://doi.org/10.1029/2011JA016477

Oppenheim, M. M., Sugar, G., Slowey, N. O., Bass, E., Chau, J. L., & Close, S. (2009). Remote sensing lower thermosphere wind profiles using non-specular meteor echoes. *Geophysical Research Letters*, *36*(9). doi: https://doi.org/10.1029/2009GL037353

Oppenheim, M. M., vom Endt, A. F., & Dyrud, L. P. (2000). Electrodynamics of meteor trail evolution in the equatorial e-region ionosphere. *Geophysical Research Letters*, *27*(19), 3173-3176. doi: https://doi.org/10.1029/1999GL000013

Oyama, S., Shiokawa, K., Kurihara, J., Tsuda, T. T., Nozawa, S., Ogawa, Y., ... Watkins, B. J. (2010). Lower-thermospheric wind fluctuations measured with an fpi during pulsating aurora at troms, norway. *Annales Geophysicae*, *28*(10), 1847–1857. doi: 10.5194/angeo-28-1847-2010

This article is protected by copyright. All rights reserved.

Author Manuscript

Philbrick, C. P., Yang, F., Vargas, F. A., Swenson, G. R., & Liu, A. Z. (2021). A na density lidar method and measurements of turbulence to 105 km at the andes lidar observatory. *Journal of Atmospheric and Solar-Terrestrial Physics*, *219*, 105642. doi: https://doi.org/10.1016/j.jastp.2021.105642

Picone, J. M., Hedin, A. E., Drob, D. P., & Aikin, A. C. (2002). Nrlmsise-00 empirical model of the atmosphere: Statistical comparisons and scientific issues. *Journal of Geophysical Research: Space Physics*, *107*(A12), SIA 15-1-SIA 15-16. doi: https://doi.org/10.1029/2002JA009430

Prlss, G. W. (1980). Magnetic storm associated perturbations of the upper atmosphere: Recent results obtained by satellite-borne gas analyzers. *Reviews of Geophysics*, *18*(1), 183-202. doi: https://doi.org/10.1029/RG018i001p00183

Richmond, A. D. (1995). Ionosphere electrodynamics using apex coordinates. *Journal of Geomagnetism and Geoelectricity*, *47*, 191-212. doi: https://doi.org/10.5636/jgg.47.191

Ridley, A. J., Deng., Y., & Tóth, G. (2006). The global ionosphere thermosphere model. *Journal of Atmospheric and Solar-Terrestrial Physics*, *68*, 839864.

Rishbeth, H., & Müller-Wodarg, I. C. F. (1999). Vertical circulation and thermospheric composition: a modeling study. *Ann. Geophysicae*, *17*(794805).

Smith, R. W. (1998). Vertical winds: a tutorial. *J. Atmos. Sol. Terr. Phys.*, *60*, 14251434.

Strugarek, D., Sonica, K., & Jggi, A. (2019). Characteristics of goce orbits based on satellite laser ranging. *Advances in Space Research*, *63*(1), 417-431. doi: https://doi.org/10.1016/j.asr.2018.08.033

Touboul, P. (2003). Microscope instrument development, lessons for goce. *Space Science Reviews*, *108*, 393-408.

Vichare, G., Ridley, A., & Yiit, E. (2012). Quiet-time low latitude ionospheric electrodynamics in the non-hydrostatic global ionospherethermosphere model. *Journal of Atmospheric and Solar-Terrestrial Physics*, *80*, 161-172. doi: https://doi.org/10.1016/j.jastp.2012.01.009

Visser, T., Doornbos, E., de Visser, C., Visser, P., & Fritsche, B. (2018). Torque model verification for the goce satellite. *Advances in Space Research*, *62*, 11141136.

Visser, T., March, G., Doornbos, E., de Visser, C., & Visser, P. (2019a). Horizontal and vertical thermospheric cross-wind from goce linear and angular accelerations. *Advances in Space Research*, *63*(10), 3139-3153. doi: https://doi.org/10.1016/j.asr.2019.01.030

Visser, T., March, G., Doornbos, E. N., de Visser, C. C., & Visser, P. N. A. M. (2019b). Characterization of thermospheric vertical wind activity at 225-km to 295-km altitude using goce data and validation against explorer missions. *J. Geophys. Res.: Sp. Phys.*, *124*, 48524869.

Wang, W., Burns, A. G., Wiltberger, M., Solomon, S. C., & Killeen, T. L. (2008). Altitude variation of the horizontal thermospheric winds during geomagnetic storms. *Journal of Geophysical Research: Space Physics*, *113*.

Wang, W., Killeen, T. L., Burns, A. G., & Roble, R. G. (1999). A high resolution, threedimensional, time dependent, nested grid model of the coupled thermosphereionosphere. , *61*, 385-397.

Weimer, D. R. (2005). Improved ionospheric electrodynamic models and application to calculating joule heating rates. *Journal of Geophysical Research: Space Physics*, *110*(A5). doi: https://doi.org/10.1029/2004JA010884

Weygand, J. M., Zesta, E., & Troshichev, O. (2014). Auroral electrojet indices in the northern and southern hemispheres: A statistical comparison. *Journal of Geophysical Research: Space Physics*, *119*(6), 4819-4840. doi: https://doi.org/10.1002/2013JA019377

Wiltberger, M., Wang, W., Burns, A. G., Burns, S. C., Solomon, S. C., Lyon, J. G., & Goodrich, C. C. (2004). Initial results from the coupled magnetosphere

This article is protected by copyright. All rights reserved.

ionosphere thermosphere model: Magnetospheric amd ionospheric responses. *Journal of Atmospheric and Solar-Terrestrial Phyics*, *66*, 1411-1424.

Yao, X., Yu, T., Zhao, B., Yu, Y., Liu, L., Ning, B., & Wan, W. (2015). Climatological modeling of horizontal winds in the mesosphere and lower thermosphere over a mid-latitude station in china. *Advances in Space Research*, *56*(7), 1354-1365. doi: https://doi.org/10.1016/j.asr.2015.06.026

Yiit, E., & Ridley, A. J. (2011). Role of variability in determining the vertical wind speeds and structure. *J. Geophys. Res.*, *116*(A12305).

Yuan, W., Liu, X., Xu, J., Zhou, Q., Jiang, G., & Ma, R. (2013). Fpi observations of nighttime mesospheric and thermospheric winds in china and their comparisons with hwm07. *Annales Geophysicae*, *31*(8), 1365-1378. doi: 10.5194/angeo-31-1365-2013

Zhao, S., Urbina, J., Dyrud, L., & Seal, R. (2011). Multilayer detection and classification of specular and nonspecular meteor trails. *Radio Science*, *46*(6). doi: https://doi.org/10.1029/2010RS004548

This article is protected by copyright. All rights reserved.

Author Manuscript